Fluid Dynamics &
Materials Processing

Tech Science Press

http://doi.org/10.32604/fdmp.2026.084304

ARTICLE

CFD-Guided Structural Optimization of Blast Furnace Gas Fine Desulfurization Systems

Chuang Guan[1,2], Wei Fu[3], Guodong Cai[1], Fengling Yang[1], Jiangtao Liu[1], Hangyu Wu[1], Chuantao Wu[1], Chunyu Zhang[1] and Ming Gao[2,*]

[1]Shandong Guoshun Construction Group Co., Ltd., Jinan, China
[2]School of Nuclear Science, Energy and Power, Shandong University, Jinan, China
[3]Zaozhuang Bayi Coal Water Slurry Thermal Power Co., Ltd., Zaozhuang, China
*Corresponding Author: Ming Gao. Email: gm@sdu.edu.cn

Received: 20 April 2026; Accepted: 24 July 2026; Published: 04 September 2026

ABSTRACT: Flow maldistribution and local short-circuiting within blast furnace gas fine desulfurization systems can substantially impair desulfurization performance while increasing hydraulic losses and energy consumption. To elucidate the underlying flow mechanisms, a three-dimensional computational fluid dynamics (CFD) model accounting for the pressure variation across the top gas recovery turbine (TRT) was developed to investigate the flow characteristics under both high- and low-pressure operating conditions. Guided by the numerical analysis, an integrated structural optimization strategy, combining inlet deflector plates with the sealing of perforated plates adjacent to partition regions, was proposed. The optimized configuration significantly enhanced flow uniformity throughout the system. Flow distribution deviations were reduced to within ±0.30% in the low-pressure section and to approximately ±3.85% in the high-pressure section during operation of the central tower. Correspondingly, the average velocity uniformity index increased from 0.82 to 0.97 in the low-pressure section and from 0.76 to 0.92 in the high-pressure section. The predicted gas residence time in the low-pressure section reached approximately 8.6 s, promoting prolonged gas-solid contact and thereby improving the conditions for sulfur removal. The simulations further demonstrate that operating pressure exerts a decisive influence on the flow field: the high-pressure section is considerably more susceptible to flow maldistribution and localized jet impingement, whereas the low-pressure section exhibits a more stable and homogeneous flow structure. Overall, the proposed optimization strategy effectively mitigates flow non-uniformity while simultaneously improving hydraulic performance, providing a robust design framework for achieving low-resistance, high-efficiency blast furnace gas fine desulfurization systems.

KEYWORDS: Blast furnace gas; fine desulfurization; numerical simulation; flow field optimization

1 Introduction

As a primary byproduct of the iron and steelmaking process, the efficient purification of blast furnace gas (BFG) represents a pivotal component in achieving the green development of the steel industry. Driven by the global transition toward low-carbon steel production and increasingly stringent environmental regulations on industrial emissions, the requirements for removing sulfur-containing pollutants from blast furnace gas (BFG) have become progressively more stringent [1]. The typical composition of BFG consists of CO (25.0%–30.0%), H_2 (1.5%–3.0%), N_2 (55.0%–60.0%), and sulfur compounds (60–160 mg/m^3). Within the total sulfur content, both inorganic sulfur (predominantly H_2S) and organic sulfur (primarily COS) coexist [2].

Copyright © 2026 The Authors. Published by Tech Science Press. This work is licensed under a Creative Commons Attribution 4.0 International License, which permits unrestricted use, distribution, and reproduction in any medium, provided the original work is properly cited.

The core of the BFG fine desulfurization process lies in achieving high-efficiency removal of COS and H_2S; a schematic diagram of a conventional BFG fine desulfurization system is illustrated in Fig. 1. Currently, the predominant technical route adheres to the principle of "hydrolysis followed by desulfurization." Specifically, COS is first converted into more manageable H_2S via hydrolysis catalysts, after which total sulfur is removed through processes such as wet oxidation, amine absorption, or dry adsorption [3–5].

Park et al. [6] developed a continuous hot gas desulfurization system based on Zn-based solid sorbents. Testing for over 30 h demonstrated that this system can achieve efficient removal of H_2S and COS at high temperatures exceeding 500°C. In the hydrolysis stage, catalysts that possess both high- and low-temperature activity along with oxidation resistance are current research hotspots. Li et al. [7] synthesized a $Cu_7Zr_3K@TiO_2$ bifunctional catalyst capable of the simultaneous removal of COS and H_2S at low temperatures. This catalyst reached a combined desulfurization capacity of 302.9 mg/g in simulated industrial gas, exhibiting promising prospects for industrial application. Furthermore, the development of novel formulated solvents also contributes to improving sulfur selectivity and desulfurization precision [8–10].

As the central functional unit of the gas purification process, the uniformity of the internal flow field distribution within the fine desulfurization system is intrinsically linked to the utilization efficiency of desulfurization agents, the operational stability of the system, and energy consumption levels [11]. Consequently, process simulation serves as an effective tool to guide process optimization.

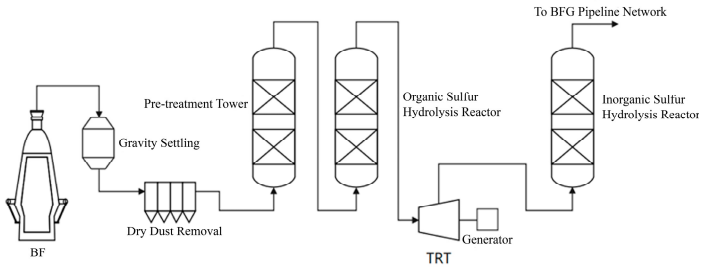

Figure 1: Process Flow Diagram (PFD) for BFG fine desulfurization.

Carneiro et al. [12] conducted a simulation study on H_2S removal from coke oven gas (COG) and validated the results with industrial data, leading to a 5.0% improvement in H_2S removal efficiency and a reduction in raw material costs by over 15.0%. Cao et al. [13]. developed a Cu/zeolite hybrid adsorbent (DSZ-2) with high sulfur capacity for H_2S removal from BFG, enabling low-temperature *in-situ* regeneration and excellent cyclic performance. Furthermore, focusing on the pre-combustion desulfurization of BFG, Jia et a [14]. improved COS hydrolysis in high-humidity BFG by physically mixing K_2CO_3/Al_2O_3 with hydrophobic PDVB, significantly enhancing low-temperature catalytic efficiency.

In addition, CFD simulation, transport mechanism analysis, and thermodynamic modeling have been increasingly applied to optimize industrial gas purification systems. Liu et al. [15] improved the flow field and desulfurization performance of a spray dispersion tower through CFD-based optimization. Aldalawy et al. [16] investigated mass transfer characteristics in porous media using combined experiments and modeling, while Yu et al. [17] and Huang et al. [18] analyzed the engineering reliability and thermodynamic performance of gas purification systems, respectively. These studies have provided valuable guidance for process optimization and system design, but their application to BFG fine desulfurization systems remains limited.

However, limitations persist in current research regarding the application of BFG fine desulfurization systems. First, the majority of studies focus on conventional desulfurization towers or isolated com-

ponents [19,20], paying insufficient attention to the unique operating conditions characterized by the substantial pressure gradient across the Top Gas Pressure Recovery Turbine (TRT) (e.g., approximately 235 kPa on the high-pressure side versus 15 kPa on the low-pressure side). A magnitude-level shift in pressure leads to significant variations in thermophysical properties, such as gas density and viscosity, thereby altering the flow field structure. Nevertheless, existing models frequently employ the assumption of constant physical properties, which may introduce considerable deviations.

Second, existing literature often treats the high-pressure subsystem upstream of the TRT and the low-pressure subsystem downstream as separate entities, lacking comparative and correlative investigations. This makes it difficult to elucidate the underlying mechanisms by which disparate pressure levels influence flow characteristics and system performance.

Third, structural optimization methods, such as the arrangement of guide vanes and pressure plates, largely rely on empirical trial-and-error. There is a notable absence of design methodologies directly coupled with quantitative flow field indicators, and comprehensive synergistic optimization strategies have yet to be fully developed.

To address the aforementioned challenges, this study constructs a three-dimensional (3D) numerical model of a BFG fine desulfurization system that explicitly accounts for pressure variations across the TRT. By incorporating variable thermophysical properties that fluctuate with local pressure and temperature, a comparative analysis of flow characteristics under diverse operating pressures is performed. On this basis, the governing laws describing the impact of pressure fluctuations on flow field distribution are elucidated, and structural optimization schemes involving guide vanes and orifice plate blockage are proposed. The research findings provide a robust theoretical and practical reference for the optimized design, energy conservation, and consumption reduction of BFG fine desulfurization systems.

2 Physical Models and Research Methods

2.1 Physical Models

Taking a specific BFG fine desulfurization system as the research subject, this study developed 3D numerical models for the sections upstream (high-pressure side) and downstream (low-pressure side) of the TRT, respectively. These models were utilized to conduct comparative analyses of the system's performance under various pressure operating conditions. The geometric configurations and the proposed optimization schemes are illustrated in Figs. 2 and 3. The core equipment assembly comprises a dechlorination tower, a hydrolysis tower, and a desulfurization tower. Furthermore, critical components-including connecting pipelines, elbows, internal packing layers, distribution plates, and collectors-are explicitly incorporated into the model.

To address the issue of flow maldistribution in the BFG fine desulfurization system, the following optimization measures are proposed. In the high-pressure zone, three guide vanes are installed within each of the inlet elbows of the dechlorination and hydrolysis towers; furthermore, the packing orifice plates are blocked within a range of 500 mm above and below the partition plate. In the low-pressure zone, three guide vanes are arranged in the inlet elbow of the desulfurization tower, while the packing orifice plates within a range of 800 mm above and below the partition plate are sealed. These measures aim to enhance gas flow distribution and suppress short-circuit flow.

It should be noted that the structural scheme proposed in this study is an engineering optimization relative to the original tower configuration, rather than a full parametric or global optimization of all geometric parameters. The three-guide-vane arrangement was selected based on the diagnosis of the original inlet-elbow flow deviation, engineering experience in elbow flow rectification, and the available

installation space in the existing industrial system. The sealing ranges of 500 mm in the high-pressure zone and 800 mm in the low-pressure zone were determined according to the observed short-circuiting tendency near the partition plates and the geometric differences between the two subsystems. The larger sealing range in the low-pressure zone was adopted because the gas momentum is lower and the flow field is more stable, allowing stronger redistribution near the partition plate without causing severe additional flow resistance.

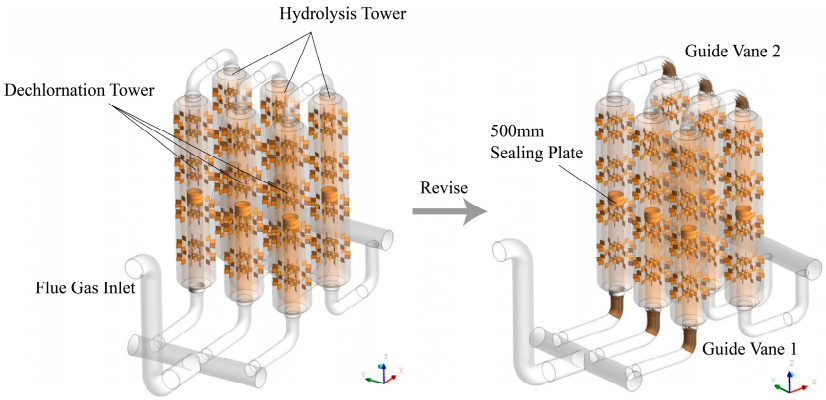

Figure 2: Optimization of the high-pressure reaction tower.

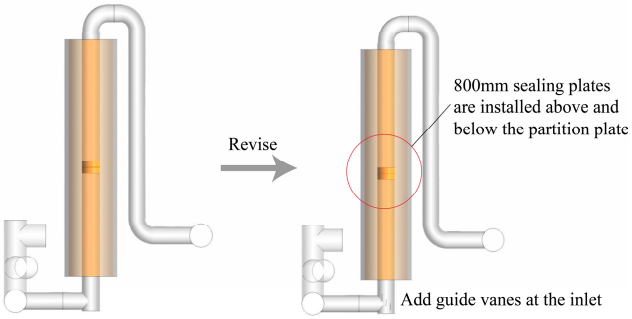

Figure 3: Optimization of the low-pressure reaction tower.

2.2 Mathematical Models

2.2.1 Assumptions

To simplify the computational complexity and highlight the primary characteristics of the system's flow and mass transfer processes, the following assumptions are made during the modeling process:

(1) Blast furnace gas (BFG) is treated as a compressible ideal gas mixture with uniformly distributed components, and the gas phase is considered a continuum.
(2) The system is assumed to be well-sealed during operation; therefore, the effects of air leakage and external gas entrainment are neglected.
(3) The gas flow and reaction processes are assumed to be in a macroscopic steady state.
(4) Heat exchange between the computational domain and the ambient environment is neglected; therefore, the gas flow process is assumed to be adiabatic.

2.2.2 Governing Equations and Turbulence Models

The gas flow inside the blast furnace gas (BFG) fine desulfurization system was simulated using the steady-state Reynolds-averaged Navier-Stokes (RANS) equations. In the RANS formulation, the instantaneous flow variables are decomposed into time-averaged and fluctuating components, and the effects of turbulence are represented through the Reynolds stresses, which require closure by an appropriate turbulence model [21].

For a compressible fluid, the steady-state continuity equation is expressed as:

$$\frac{\partial(\rho u_i)}{\partial x_i} = 0 \tag{1}$$

where ρ is the fluid density, kg/m^3; u_i is the time-averaged velocity component, m/s; x_i denotes the coordinate direction.

The corresponding Reynolds-averaged momentum equation is:

$$\frac{\partial(\rho u_i u_j)}{\partial x_i} = \frac{\partial}{\partial x_i}[\mu(\frac{\partial u_i}{\partial x_j} + \frac{\partial u_j}{\partial x_i} - \frac{2}{3}\delta_{ij}\frac{\partial u_k}{\partial x_k})] - \frac{\partial p}{\partial x_i} + \frac{\partial(-\rho\overline{u_i' u_j'})}{\partial x_j} \tag{2}$$

where p is the static pressure (Pa), μ is the dynamic viscosity (Pa·s), and $-\rho\overline{u_i' u_j'}$ denotes the Reynolds stress tensor generated by turbulent fluctuations.

To close the Reynolds stress term, the Realizable k-ε turbulence model proposed by Hou et al. [22] was adopted. Compared with the Standard k-ε model, the Realizable k-ε model employs a variable model coefficient and a modified transport equation for the turbulent dissipation rate, thereby improving the prediction of flow separation, streamline curvature, recirculation, and rotational flows while maintaining relatively low computational cost. Since the present study mainly focuses on the overall flow distribution, pressure loss, and velocity uniformity in a large-scale industrial gas purification system rather than detailed near-wall turbulence structures, the Realizable k-ε model provides a reasonable balance between computational accuracy and computational efficiency.

The transport equation for turbulent kinetic energy k is given by:

$$\frac{\partial(\rho k)}{\partial t} + \frac{\partial(\rho k u_i)}{\partial x_i} = \frac{\partial}{\partial x_j}[(\mu + \frac{\mu_t}{\sigma_k})\frac{\partial k}{\partial x_j}] + G_k - \rho\varepsilon \tag{3}$$

where k is the turbulent kinetic energy (m^2·s^{-2}), μ_t is the turbulent viscosity (Pa·s), G_k represents the production of turbulent kinetic energy caused by the mean velocity gradients, σ_k is the turbulent Prandtl number for k, and ε is the turbulent dissipation rate (m^2·s^{-2}).

The transport equation for the turbulent dissipation rate ε is:

$$\frac{\partial(\rho\varepsilon)}{\partial t} + \frac{\partial(\rho\varepsilon u_i)}{\partial x_i} = \frac{\partial}{\partial x_j}[(\mu + \frac{\mu_t}{\sigma_\varepsilon})\frac{\partial\varepsilon}{\partial x_j}] + \rho C_1 S\varepsilon - \rho C_2\frac{\varepsilon^2}{k + \sqrt{\nu\varepsilon}} \tag{4}$$

where S is the modulus of the mean strain rate, (s^{-1}), ν is the kinematic viscosity (m^2·s^{-1}), and σ_ε is the turbulent Prandtl number for ε. In the realizable k-ε model, C_1 is not a constant but is calculated as:

$$C_1 = \max(0.43, \frac{\eta}{\eta + 5}), \eta = \frac{Sk}{\varepsilon} \tag{5}$$

The model constants used in the present simulation were C_2 = 1.90, σ_ε = 1.20.

The turbulent viscosity is calculated as:

$$\mu_t = \rho C_\mu \frac{k^2}{\varepsilon} \tag{6}$$

where C_μ is not a constant but is determined dynamically according to the realizability constraint of the turbulence model [4]:

$$C_\mu = \frac{1}{A_0 + A_s(kU^*/\varepsilon)} \tag{7}$$

where A_0 = 4.04, while A_s and U^* are functions of the local mean strain and rotation tensors. Thus, all turbulence-model coefficients were calculated using the default formulation of the realizable k-ε model implemented in ANSYS Fluent.

In the present simulations, the Realizable k-ε model implemented in ANSYS Fluent was employed together with the standard wall function to resolve the near-wall flow. Considering that the main objective of this study is to investigate the global flow distribution, pressure loss, and flow uniformity under different operating pressures, rather than detailed boundary-layer behavior, this turbulence model has been demonstrated to provide reliable predictions for engineering-scale gas-flow systems while maintaining good computational efficiency [23].

2.2.3 Variable Physical Property Models

To accurately simulate the effects of the drastic pressure drop across the TRT-descending from 235 kPa to 15 kPa-on gas thermophysical properties and the resulting flow field, variable property parameters are incorporated into the present model.

Density equation for a gas mixture:

$$\rho = \frac{p_0 M_{mix}}{R T_0} \tag{8}$$

where p_0 is the local absolute pressure, Pa, T_0 is the local temperature, K, M_{mix} is the instantaneous average molar mass of the gas mixture, kg/mol; and R is the universal gas constant, taken as 8.314 J/(mol·K).

The viscosity of a mixture can be calculated using the Wilke mixture equation [24]:

$$\mu = \sum_i \frac{x_i \mu_i}{\sum_j x_j \phi_{ij}} \tag{9}$$

Among these:

$$\phi_{ij} = \frac{1}{\sqrt{8}}\left(1 + \frac{M_i}{M_j}\right)^{-1/2}\left[1 + \left(\frac{\mu_i}{\mu_j}\right)^{1/2}\left(\frac{M_j}{M_i}\right)^{1/4}\right]^2 \tag{10}$$

where μ_i is the dynamic viscosity of the i_{th} component, Pa·s, M_i is the molar mass of the i_{th} component, kg/mol; and ϕ_{ij} is the interaction parameter between components.

The viscosity of the pure component is expressed using the Sutherland equation [25]:

$$\mu_i = \mu_{i,0}\left(\frac{T}{T_0}\right)^{3/2} \frac{T_0 + S_i}{T + S_i} \tag{11}$$

where $\mu_{i,0}$ is the dynamic viscosity of the i_{th} component at the reference temperature, Pa·s, and S_i is the Sutherland constant, taken as 110.4 K.

The pressure variation across the TRT mainly influences the gas density. According to the ideal-gas mixture equation, the density is directly related to local pressure and temperature; therefore, the large pressure difference between the high-pressure and low-pressure zones can significantly affect gas momentum, pressure loss, and flow redistribution. By contrast, the dynamic viscosity calculated using the Wilke mixture rule and the Sutherland equation is mainly affected by gas composition and temperature, while its pressure dependence is relatively weak under the present operating conditions. Accordingly, pressure-dependent density and temperature-dependent viscosity were adopted in the CFD model.

2.3 Numerical Computation Methods

The numerical solution in this study is implemented using the ANSYS Fluent steady-state solver. The pressure-velocity coupling is handled via the SIMPLE algorithm. Second-order upwind schemes are employed for the discretization of the convection terms and turbulence-related equations, while the central difference scheme is applied to the diffusion terms. The under-relaxation factors are specified as follows: 0.3 for pressure, 0.7 for momentum, and 0.8 for turbulence and species, respectively. The convergence criteria for the residuals of all governing equations are set to 10^{-6}. Additionally, a comprehensive assessment of computational convergence is performed by monitoring the stability of the total pressure at the outlet.

The boundary conditions for the computational domain are defined based on the characteristics of the actual operating conditions: (1) Inlet Conditions: A mass flow inlet is employed, with the total flow rate of BFG set to 330,000 Nm^3/h. The mass fractions of individual components are specified according to actual process data, and a velocity profile is configured to accurately simulate inlet effects. (2) Outlet Conditions: A pressure outlet is utilized. For the two comparative scenarios (upstream and downstream of the TRT), the outlet static pressures are set at 235 kPa and 15 kPa, respectively. (3) Wall Conditions: A no-slip boundary condition is applied to all solid walls, and standard wall functions are used to resolve the flow and turbulence within the near-wall region.

A polyhedral meshing approach is adopted, with local refinement applied to critical regions such as reactor internals and pipe elbows. To resolve the near-wall flow, boundary layer meshes are generated to ensure that the dimensionless wall distance, y^+ remains within the range of 30–300, thereby satisfying the requirements of the standard wall functions. The final generated mesh system is illustrated in Fig. 4.

Figure 4: Schematic diagram of the model grid.

To ensure that the numerical results were independent of the mesh density, a mesh independence study was carried out using four mesh systems with different element numbers. The total pressure drop of the system was selected as the main evaluation parameter because it directly reflects the overall flow

resistance characteristics of the BFG fine desulfurization system. As shown in Table 1, the total pressure drop gradually stabilizes with increasing mesh number. When the number of elements increases from approximately 3.16 million to 3.67 million, the total pressure drops almost unchanged, indicating that further mesh refinement has only a limited influence on the numerical results. Therefore, considering both computational accuracy and computational cost, the mesh system with approximately 3.16 million elements was selected for the subsequent simulations.

Table 1: Mesh independence test based on the total pressure drop.

Mesh Case	Number of Elements/million	Total Pressure Drop/Pa
1	2.32	2938
2	2.84	3150
3	3.16	3214
4	3.67	3227

2.4 Model Validation

To verify the reliability of the mathematical model and the specified parameters, the simulation results for a typical design condition on the high-pressure side upstream of the TRT (inlet temperature of 140°C and pressure of 235 kPa) were compared with field operational data. As summarized in Table 2, the simulated total flow resistance loss of the system under this condition is 3214 Pa, including approximately 1700 Pa from the packing layer and 1514 Pa from frictional and local losses in the piping. The corresponding measured total flow resistance loss obtained from field operational data is 3080 Pa. The relative error between the simulated and measured values is 4.3%, which is within an acceptable range for engineering applications. In addition to the total flow resistance loss, the averaged gas velocity at the outlet section of the packing layer was further used to validate the numerical model, as shown in Table 1. This parameter is directly related to the gas-flow magnitude in the main reaction region and can be derived from plant operating data. These results demonstrate that the established numerical model accurately reflects the actual flow resistance characteristics of the piping system and is suitable for subsequent operating condition analysis and optimization studies.

Table 2: Comparison of model validation results.

Comparison of Parameters	Simulated Value	Measured Value	Relative Error
Total flow resistance loss (Pa)	3214	3080	4.3%
Averaged velocity at outlet	4.2	4.0	4.8%

2.5 Speed Uniformity Evaluation Criteria

To quantitatively characterize the uniformity of gas flow distribution and its evolutionary patterns along the flow path in the BFG fine desulfurization system, a velocity uniformity coefficient K_u over a given cross-section is introduced during the post-processing of numerical results. This coefficient, defined by Eq. (7), serves to provide a quantitative evaluation of the velocity distribution:

$$K_u = 1 - \sqrt{\sum_{i=1}^{n} \left(\frac{v_i - \overline{v}}{\overline{v}}\right)^2 A_i / \sum_{i=1}^{n} A_i} \tag{12}$$

where v_i is the local velocity of the i_{th} element on the cross-section (taking the velocity component in the mainstream direction); A_i is the area of the corresponding element; and n is the number of discrete elements on the cross-section; and $\bar{v}$ is the area-weighted mean velocity over the cross-section, m/s.

This coefficient reflects the degree of deviation (or dispersion) of the cross-sectional velocity distribution relative to the mean velocity. The value of K_u ranges from 0 to 1. A value closer to 1 indicates a more uniform velocity distribution across the section; conversely, a lower value signifies the presence of significant.

3 Results and Discussions

3.1 Optimization Study of the Piping System in the High-Pressure Zone Upstream of the TRT

To evaluate the impact of structural optimization on the flow characteristics within the high-pressure zone, a comparative analysis of the velocity and pressure fields before and after optimization was conducted, as illustrated in Figs. 5 and 6.

As shown in Fig. 5, prior to optimization, the gas flow exhibits a pronounced flow deviation within the inlet elbow and the distribution region upstream of the tower. This results in an inhomogeneous flow field characterized by high local velocities in some areas and sluggish flow in others. Furthermore, a short-circuiting tendency is observed near the partition plate, which prevents the gas from being fully distributed within the packing layer.

After optimization, by installing guide vanes in the inlet elbow and sealing the orifice plates near the partition plate, the gas flow direction is effectively rectified. The streamline distribution becomes more uniform and continuous; specifically, the high-velocity zones are significantly attenuated, the low-velocity regions are reduced, and the flow integration within the packing zone is substantially enhanced. Consequently, the overall uniformity of the flow field is markedly improved.

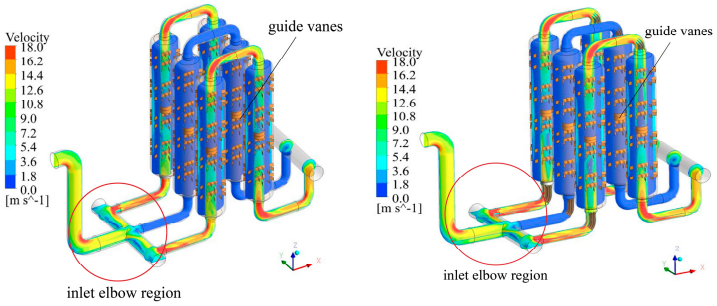

Figure 5: Comparison of velocity fields in the high-pressure zone before and after flow-path optimization (**a**) Original configuration; (**b**) Revised configuration.

According to the pressure field distribution in Fig. 6, the system prior to optimization exhibits intense pressure gradients at the elbows and regions with abrupt structural changes, resulting in non-uniform pressure distribution and high local resistance losses. After optimization, the installation of guide vanes mitigates the secondary flow and local impingement effects at the elbows, leading to a smoother pressure distribution and a more reasonable overall pressure drop.

The resistance losses in the high-pressure zone vary under different operating modes: when the two side absorption towers are in operation with the central tower on standby, the total system resistance is approximately 3214 Pa, comprising a packing layer resistance of 1700 Pa and a piping resistance of 1514 Pa. When the central tower is commissioned (put into operation), the total resistance decreases to

approximately 2928 Pa, with the piping resistance reduced to 1228 Pa. This indicates that changes in the flow path have a significant impact on the system's flow resistance.

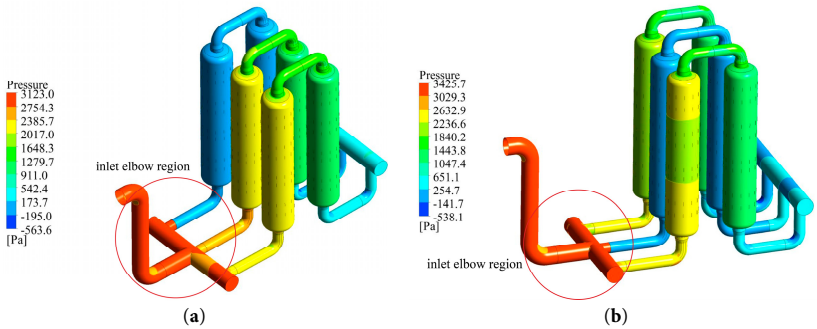

Figure 6: Comparison of pressure fields in the high-pressure zone before and after flow-path optimization: (**a**) Original configuration; (**b**) Revised configuration.

Further analysis from the perspective of flow distribution reveals that, under full-open valve conditions, the distribution characteristics in the high-pressure zone are significantly influenced by the tower operating configuration. When the two side towers are in operation with the central tower on standby, the BFG is distributed relatively uniformly with minimal variation between towers. However, when the central tower is commissioned and the side towers are partially on standby, the flow maldistribution increases to approximately ±3.85%, with the central tower exhibiting a higher flow rate.

This phenomenon is primarily attributed to the high gas momentum under high-pressure conditions, which makes the flow direction more sensitive to the configuration of the inlet piping structure, thereby leading to flow concentration (biasing). Furthermore, the inlet damper of the central tower is subjected to substantial pressure, posing a potential risk to structural integrity.

Building upon the aforementioned qualitative analysis, to further quantify the impact of structural optimization on the flow field uniformity in the high-pressure zone, a statistical analysis was performed on several characteristic cross-sections along the mainstream direction, utilizing the velocity uniformity coefficient K_u defined before. Fig. 6 illustrates the evolution of the velocity uniformity coefficient, K_u, relative to the position along the flow path before and after optimization. For ease of comparison, the flow path length is normalized into a percentage of distance along the trajectory (where 0% represents the inlet of the inlet elbow and 100% represents the outlet section).

As illustrated in the Fig. 7 below, in the original configuration of the high-pressure zone, the velocity distribution deteriorates rapidly after the inlet elbow due to inertial effects and abrupt structural changes. The uniformity coefficient reaches its minimum of only 0.55 at the 20% position, indicating the presence of pronounced flow biasing and localized high-velocity zones. This observation is consistent with the flow concentration phenomenon at the elbow exit previously identified in the velocity contours.

After optimization, with the installation of guide vanes in the inlet elbow, the gas flow is effectively rectified before entering the distribution region. Consequently, the uniformity coefficient at the 20% position significantly increases to 0.78, representing an improvement of approximately 41.8% compared to the original configuration. Subsequently, the uniformity continues to improve along the flow path, reaching 0.92 before entering the packing layer (at the 100% position)—a 21.1% increase over the baseline value of 0.76. These results demonstrate that the optimization measures effectively suppress the development of flow biasing and facilitate the homogenization of the flow field.

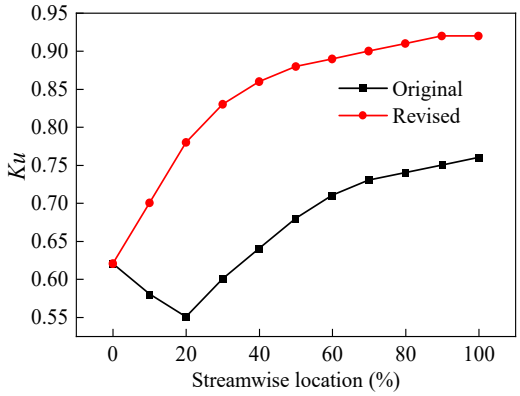

Figure 7: Comparison of velocity uniformity coefficients along the flow path in the high-pressure zone.

Furthermore, the uniformity recovery process in the original configuration of the high-pressure zone is relatively slow. In contrast, the optimized configuration exhibits a rapid enhancement in uniformity within the 30%–60% section, indicating that the flow-guiding structures play a pivotal role in the fluid redistribution process. However, due to the substantial gas momentum under high-pressure conditions, a certain degree of residual non-uniformity persists. This finding is consistent with the previously discussed analysis of flow distribution deviations.

In summary, the structural optimization of the high-pressure zone significantly enhances flow field uniformity and optimizes pressure distribution characteristics by improving the inlet flow conditions and suppressing short-circuiting flow. However, challenges such as flow maldistribution under varying operating modes and localized pressure-bearing issues persist. It is therefore necessary to further refine the system's operational strategies by considering the pressure-bearing capacity of the dampers and incorporating field control measures (e.g., installing flow meters and control valves or further optimizing the piping structure).

3.2 Optimization Study of the Piping System in the Low-Pressure Zone Downstream of the TRT

To analyze the impact of structural optimization on the flow characteristics in the low-pressure zone, a comparative study of the velocity and pressure fields before and after optimization was performed, as illustrated in Figs. 8 and 9.

As illustrated in Fig. 8, prior to optimization, the gas flow exhibits a certain degree of velocity non-uniformity within the inlet elbow and the distribution region upstream of the tower. Localized high-velocity biasing occurs, while some areas within the packing layer experience lower velocities; this uneven gas distribution compromises the gas-solid contact efficiency.

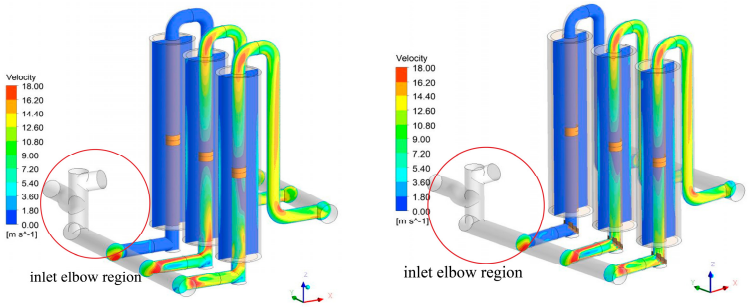

Figure 8: Comparison of velocity fields in the low-pressure zone before and after flow-path optimization: (**a**) Original configuration; (**b**) Revised configuration.

After optimization, by installing guide vanes in the inlet elbow and sealing the orifice plates near the partition plate, the gas flow path is effectively reconfigured. The gas distribution becomes more uniform, with streamlines appearing smoother and more continuous. The high-velocity zones are markedly attenuated, and the low-velocity stagnant zones are significantly reduced. Consequently, the gas distribution within the packing layer is more balanced, leading to a substantial improvement in the overall uniformity of the flow field.

Based on the pressure field distribution shown in Fig. 9, the system prior to optimization exhibits significant pressure gradients at the elbows and locations of abrupt structural changes, leading to substantial local pressure drops and increased energy dissipation.

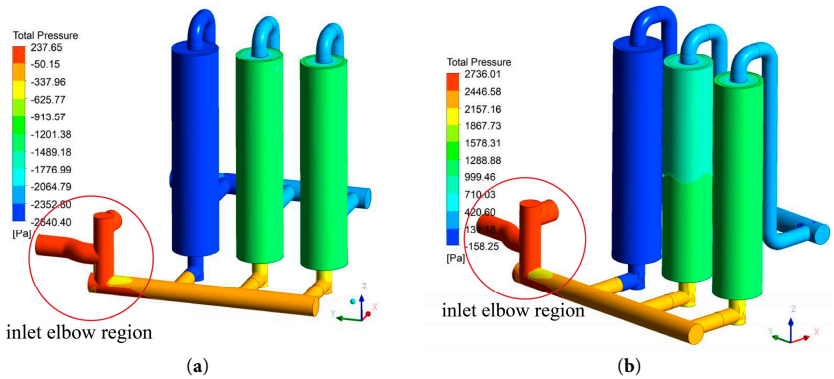

Figure 9: Comparison of pressure fields in the low-pressure zone before and after flow-path optimization: (**a**) Original configuration; (**b**) Revised configuration.

After optimization, the guiding structures effectively mitigate flow separation and local impingement effects at the elbows, resulting in a smoother pressure distribution and a more balanced pressure drop profile. In the low-pressure zone, the total system resistance is approximately 2393 Pa, with the packing layer accounting for 1400 Pa and the piping resistance contributing 993 Pa. These data indicate that the system resistance is primarily concentrated within the packing region, while the piping resistance remains relatively low, suggesting a more stable flow regime.

From the perspective of flow distribution, under full-open valve conditions, the BFG flow among the absorption towers in the low-pressure zone is relatively uniform. Following optimization, the flow distribution deviation is approximately ±0.3%, which is far superior to the engineering control requirement of ±3%. This demonstrates that the proposed synergetic optimization of guide vanes and orifice plate sealing possesses excellent applicability and stability under low-pressure conditions.

Furthermore, the superficial gas velocity within the packing layer of the low-pressure zone is approximately 0.40 m/s, corresponding to an estimated gas residence time of about 8.6 s within the desulfurization tower. This indicates that the low-pressure zone can provide a relatively longer gas-solid contact time. Such a longer contact time may be favorable for the desulfurization process. However, since no reaction-kinetics model, residence time distribution analysis, or tracer simulation was performed in the present study, the residence-time result is used only as an auxiliary indicator for evaluating the flow-field characteristics.

To quantitatively analyze the impact of structural optimization on the flow field uniformity within the low-pressure zone, the velocity uniformity coefficients at various characteristic cross-sections along the flow path were calculated, with the results presented in Fig. 10.

As illustrated in the figure above, the overall flow field uniformity of the original configuration in the low-pressure zone is superior to that in the high-pressure zone. Its minimum value occurs at the 20%

position, indicating that under low-pressure conditions, the gas momentum is lower, and the flow response to abrupt structural changes is relatively weaker, thereby mitigating the degree of flow biasing. Before entering the packing layer (i.e., at the 100% flow path position), the velocity uniformity coefficient of the original configuration is 0.82.

After optimization, the velocity uniformity coefficient is significantly improved across the entire flow path. At the 20% position, the coefficient increases from 0.63 to 0.85, representing an enhancement of approximately 34.9%. It further rises to 0.97 before entering the packing layer, which is an 18.3% increase compared to the 0.82 of the original configuration. Simultaneously, it can be observed that the uniformity coefficient quickly stabilizes after the 30% position (K_u > 0.9). This indicates that the flow achieves effective homogenization within a relatively short distance.

Compared with the high-pressure zone, the flow field in the low-pressure zone exhibits a faster uniformity recovery and achieves a higher degree of final homogeneity. This is primarily because, under low-pressure conditions, the lower gas density results in diminished inertial effects, making the flow more susceptible to regulation by the guiding structures, thereby facilitating a more rapid homogenization. This observation is consistent with the previous analysis regarding the flow stability in the low-pressure zone.

Overall, the structural optimization of the low-pressure zone effectively improves flow field uniformity and reduces local resistance losses, resulting in more stable system operation. Compared to the high-pressure zone, the low-pressure zone exhibits lower gas density and momentum, which reduces the flow's sensitivity to structural disturbances. Consequently, uniform distribution and stable operation are more easily achieved. This further validates the adaptability and effectiveness of the proposed optimization scheme under varying pressure conditions.

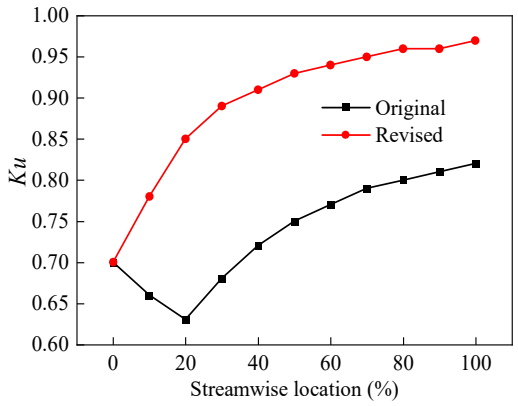

Figure 10: Comparison of velocity uniformity coefficients along the flow path in the low-pressure zone.

4 Conclusion

In this study, based on the CFD method, numerical simulations and structural optimization research were conducted on the flow characteristics of a BFG fine desulfurization system under varying pressure conditions before and after the TRT. The primary conclusions are as follows:

(1) By installing guide vanes in the inlet elbow and sealing the orifice plates near the partition plate, the flow field distribution of the system is effectively improved. This strategy successfully suppresses gas short-circuiting, leading to a significant enhancement in flow uniformity across both the high-pressure and low-pressure zones.

(2) Following optimization, the flow distribution deviation in the low-pressure zone is controlled within ±0.3%, which is significantly superior to the engineering requirement (±3%). In the high-pressure zone, however, flow distribution is more susceptible to operational modes, with a deviation of approximately ±3.85% when the middle tower is in operation, indicating that the flow is more sensitive to structural configurations under high-pressure conditions.

(3) The synergetic optimization of guide vanes and orifice plate sealing significantly improves the flow field distribution and suppresses short-circuiting flow. Specifically, the velocity uniformity coefficient increases from 0.76 to 0.92 in the high-pressure zone and from 0.82 to 0.97 in the low-pressure zone.

(4) Pressure levels exert a significant influence on the flow characteristics of the system. The high-pressure zone is prone to flow biasing and local impingement, whereas the low-pressure zone exhibits more stable flow and longer residence times, which are conducive to reaction intensification. Furthermore, the optimized system features a more rational resistance distribution, demonstrating substantial value for practical engineering applications.

Acknowledgement: Not applicable.

Funding Statement: The authors received no specific funding for this study.

Author Contributions: The authors confirm contribution to the paper as follows: conceptualization, Chuang Guan and Ming Gao; methodology, Chuang Guan; software, Chuang Guan; validation, Wei Fu; formal analysis, Wei Fu and Chuang Guan; investigation, Chuang Guan and Wei Fu; resources, Guodong Cai and Ming Gao; data curation, Wei Fu; writing—original draft preparation, Chuang Guan; writing—review and editing, Chuang Guan, Ming Gao and Fengling Yang; visualization, Chuang Guan; supervision, Ming Gao; project administration, Ming Gao; funding acquisition, Ming Gao. Jiangtao Liu, Hangyu Wu, Chuantao Wu, Chunyu Zhang, Guodong Cai and Fengling Yang contributed to the investigation, data interpretation, and manuscript revision. All authors reviewed and approved the final version of the manuscript.

Availability of Data and Materials: The data that support the findings of this study are available from the corresponding author, upon reasonable request.

Ethics Approval: Not applicable.

Conflicts of Interest: The authors declare no conflicts of interest.

References

1. Guo Y, Hou T, Wang Y, Chang L, Wang J, Liao J. COS generation behavior during desulfurization for H_2S over zeolite in simulated blast furnace gas. Chin J Chem Eng. 2026;93:279–92. [CrossRef].
2. Kan H, Wang S, Xie Z, Shen Y. Reactive CFD-DEM modelling of particle-scale gas-solid flows in an industrial ironmaking blast furnace. Chem Eng J. 2025;525:169942. [CrossRef].
3. Lin Y, Li Y, Cao Q, Wang J, Cui Y, Zhu T. Enhanced HCl resistance of Na-Ce/Al_2O_3 hydrolysis catalyst to boost blast furnace gas purification. J Clean Prod. 2025;525:146629. [CrossRef].
4. Lin Y, Li Y, Wang B, Tian J, Liu H, Li Y, et al. Pilot-scale testing on catalytic hydrolysis of carbonyl sulfur combined with absorption-oxidation of H_2S for blast furnace gas purification. J Environ Sci. 2025;151:360–72. [CrossRef].
5. Li P, Wang G, Dong Y, Zhuo Y, Fan Y. A review on desulfurization technologies of blast furnace gases. Curr Pollut Rep. 2022;8(2):189–200. [CrossRef].
6. Park YC, Jo SH, Ryu HJ, Moon JH, Yi CK, Yoon Y, et al. Simultaneous removal of H_2S and COS using Zn-based solid sorbents in the bench-scale continuous hot gas desulfurization system integrated with a coal gasifier. Korean J Chem Eng. 2012;29(12):1812–6. [CrossRef].

7. Li X, Wang X, Yuan L, Wang L, Ma Y, Wu Y, et al. COS and H_2S simultaneous removal from blast furnace gas over a tailored Cu/Zr Co-doped K@TiO_2 bifunctional catalyst under low temperature. Chem Eng J. 2023;471:144573. [CrossRef].
8. He J, Lu M, Wu X, Gou H, Zhang N, Xu Z. Synergistic removal of CO_2, H_2S and COS from blast furnace gas with a sulfolane-based biphasic absorbent: performance and mechanism. New J Chem. 2026;50:2032–43. [CrossRef].
9. He J, Gou H, Geng L, Shu H, Liu Y, Zhang L. Formulated absorbent for fine desulfurization and carbon capture of blast furnace gas based on alcohol amine solution. Environ Eng Res. 2025;30(5):240648. [CrossRef].
10. Guo Y, Du K, Luo L, Gu S, Geng N, Zhu T. Cyclic effects of sulfur deposition on CO_2 by vacuum pressure swing adsorption from blast furnace gas. Carbon Capture Sci Technol. 2025;14:100361. [CrossRef].
11. Deng Q, Ran J, Niu J, Yang Z, Pu G, Yang L. Numerical Study on Flow Field Distribution Regularities in Wet Gas Desulfurization Tower Changing Inlet Gas/Liquid Feature Parameters. J Energy Resour Technol. 2021;143(2):023005. [CrossRef].
12. de Oliveira Carneiro L, de Vasconcelos SF, de Farias Neto GW, Brito RP, Brito KD. Improving H_2S removal in the coke oven gas purification process. Sep Purif Technol. 2021;257:117862. [CrossRef].
13. Cao E, Zheng Y, Zhang H, Wang J, Li Y, Zhu T, et al. *In-situ* regenerable Cu/Zeolite adsorbent with excellent H_2S adsorption capacity for blast furnace gas. Sep Purif Technol. 2024;336:126305. [CrossRef].
14. Jia L, Zheng Y, Li Y, Zhu T, Cui Y. Physical mixing of K_2CO_3/Al_2O_3 and poly(divinylbenzene) to promote COS removal from blast furnace gas with high humidity at low temperature. Colloids Surf A Physicochem Eng Aspects. 2024;690:133854. [CrossRef].
15. Liu J, Tomassone MS, Kuang X, Zhou S. Operation parameters and design optimization based on CFD simulations on a novel spray dispersion desulfurization tower. Fuel Process Technol. 2020;209:106514. [CrossRef].
16. Aldalawy A, Abdi M, Hassanzadeh H. A new method for simultaneous measurements of binary diffusion coefficient in bulk liquids and porous media—experiment and modeling. Fluid Phase Equilib. 2026;610:114792. [CrossRef].
17. Yu Z, Wen S, Fan R, Huang G, Huang H, Yan J. Failure analysis of cracking of 316L Medium-Pressure superheated steam Piping in a natural gas purification plant. Eng Fail Anal. 2026;192:110861. [CrossRef].
18. Huang S, Huang W, Xu X, Li A, Liu X, He M, et al. Thermodynamic modeling and analysis of ionic liquid-based purification system for low-concentration coal-mine gas utilization. Energy Convers Manag. 2026;351:121052. [CrossRef].
19. Wang SJ, Zhu P, Zhang G, Zhang Q, Wang ZY, Zhao L. Numerical simulation research of flow field in ammonia-based wet flue gas desulfurization tower. J Energy Inst. 2015;88(3):284–91. [CrossRef].
20. Wang Y, Yang J, Xu Q, Zhang Q, He S, Gao M. Numerical simulation on the enhancement of heat transfer performance by deflector plates for the mechanical draft cooling towers. Energy. 2023;283:129180. [CrossRef].
21. Shih TH, Liou WW, Shabbir A, Yang Z, Zhu J. A new k-? eddy viscosity model for high Reynolds number turbulent flows. Comput Fluids. 1995;24(3):227–38. [CrossRef].
22. Hou B, Chen O, Wang Y, Wang F, Lu G. Structural optimization and flow field simulation of gas distribution device in desulfurization tower. Asia-Pacific J Chem Eng. 2024;19:e2988. [CrossRef].
23. Li Z, Qi Z, Wang Z, Ji L, Li Z. Numerical investigation of scrap charging into an ironmaking blast furnace. Energy. 2025;315:134440. [CrossRef].
24. Wilke CR. A viscosity equation for gas mixtures. J Chem Phys. 1950;18(4):517–9. [CrossRef].
25. De Vanna F, Picano F, Benini E. A sharp-interface immersed boundary method for moving objects in compressible viscous flows. Comput Fluids. 2020;201:104415. [CrossRef].